

Article

# Design Method of Double-Boost DC/DC Converter with High Voltage Gain for Electric Vehicles

Zhengxin Liu, Jiuyu Du \* and Boyang Yu

State Key Laboratory of Automotive Safety and Energy, Tsinghua University, Beijing 100084, China; liuzhengxin\_ma18@hrbust.edu.cn (Z.L.); yuboyang\_ma17@hrbust.edu.cn (B.Y.)

\* Correspondence: dujiuyu@tsinghua.edu.cn; Tel.: +86-10-6279-5488

Received: 18 September 2020; Accepted: 5 October 2020; Published: 7 October 2020



**Abstract:** Direct current to direct current (DC/DC) converters are required to have higher voltage gains in some applications for electric vehicles, high-voltage level charging systems and fuel cell electric vehicles. Therefore, it is greatly important to carry out research on high voltage gain DC/DC converters. To improve the efficiency of high voltage gain DC/DC converters and solve the problems of output voltage ripple and robustness, this paper proposes a double-boost DC/DC converter. Based on the small-signal model of the proposed converter, a double closed-loop controller with voltage–current feedback and input voltage feedforward is designed. The experimental results show that the maximum efficiency of the proposed converter exceeds 95%, and the output voltage ripple factor is 0.01. Compared with the traditional boost converter and multi-phase interleaved DC/DC converter, the proposed topology has certain advantages in terms of voltage gain, device stress, number of devices, and application of control algorithms.

**Keywords:** electric vehicle; high voltage gain; DC/DC converter; topology; efficiency

## 1. Introduction

With the problems of environmental pollution and the energy crisis becoming more and more serious, new energy vehicles (NEVs) are receiving more and more attention. However, in the case of fuel cell electric vehicles, and high-voltage level charging systems, DC/DC converters have problems such as large output voltage fluctuation [1], poor dynamic performance, and low output voltage level [2]. Therefore, in electric vehicle applications, DC/DC converters are required to achieve the goals of high voltage gain [3], voltage decoupling and power control [4].

High voltage gain DC/DC converters fall into different classifications according to their functions and topologies [5]. According to whether there is a transformer in the topology, they can be divided into isolated DC/DC converters and non-isolated DC/DC converters [6]. A non-isolated DC/DC converter has the advantages of high power density, simple structure and control [7]. Due to the transformer, the isolated converter has disadvantages such as large volume, low power density, and easy magnetic flux saturation [8]. These disadvantages may result in isolated structures being limited in electric vehicle (EV) applications [9]. Therefore, in order to improve efficiency and power density, non-isolated DC/DC converters are more desirable for the above applications [10].

In the studies of the topology of non-isolated DC/DC converters, there are mainly hybrid topologies based on basic chopper circuit expansion, switched inductor and switched capacitor topologies, cascaded topologies, and topologies based on Z-source and quasi-Z-source. A high voltage gain DC/DC converter based on a Zeta converter was proposed in [11]. Although the topology has only one main switch, switching loss and voltage stress can be reduced by selecting low resistance switching mode. A high voltage gain DC/DC cascade boost converter for fuel cell electric vehicles was presented in [12], and the output voltage is regulated by a proportional-integral (PI) controller. An improved

floating interleaved boost converter was proposed in [13], which achieves a zero-ripple input current and maintains the advantages of high voltage gain and low voltage stress. A non-coupled inductor high voltage gain DC/DC converter based on Sepic topology was presented in [14], reducing conductive loss by using a switch with a lower conductive resistance, and an additional clamping circuit is not required. This converter has some advantages such as lower voltage stress, in-phase output voltage, high efficiency, high voltage gain and continuous input current. A high voltage gain DC/DC converter that combines the main features of a secondary boost and a Cuk converter is presented in [15]. This converter requires only one switch to achieve a high step-up ratio, simplified control, and common ground at the input and output sides. In [16], a DC/DC converter with continuous input current and high voltage gain was obtained using a Sepic converter and a switched capacitor. A voltage multiplier converter based on switched capacitors was proposed in [17], and the boost ratio of this topology is twice that of conventional boost converters, while the voltage stress of the capacitors and diodes is only half of the output voltage. However, it also has the disadvantage that the input and output do not achieve common ground. The improved multiplier structure proposed in [18] achieves common ground on the input and output sides to avoid electromagnetic interference in engineering applications. A cascade topology for fuel cell applications is presented in [19], which consists of two staggered boost converters as the first stage and a three-level boost converter selected as the second stage. The interleaved structure can reduce the input current ripple, and the three-level structure can reduce the switching loss and improve the converter efficiency. A series of step-up DC/DC converters with cascaded quasi-z-source networks were proposed in [20] to implement a bipolar quasi-z-source converter. Compared to the conventional quasi-z-source topology, the duty cycle of this topology is reduced by 30% for the same voltage gain. The input of the four-phase interleaving DC/DC converter consists of four inductor parallel connections, which can reduce the input current ripple. Output capacitors connected in series can greatly improve the voltage gain of the converter; the four power switches are turned on sequentially at 90° electrical angle intervals, reducing the input current ripple and the output voltage ripple [21]. A topology using a four-switch buck–boost converter was proposed in [22]. Based on an equivalent model of its high-frequency switching network, a double-zero triode compensator and a fractional proportional-integral-derivative (PID) controller were designed to achieve the output regulation of the fuel cell system. In [23], a nonlinear robust controller and a proportional integration controller are proposed to regulate the output voltage of the interleaved boost converter (IBC) converter using a particle swarm optimization algorithm. The experimental results show that the proposed control strategy is superior in terms of robustness, traceability and responsiveness. In [24], the vector decoupling and parameter tuning of the EV charging system is achieved using a hybrid of particle swarm optimization and artificial physical optimization. A system based on a conventional bidirectional boost converter is validated using hardware-in-the-loop devices. The experimental results show that the proposed algorithm has good robustness and effectiveness. In [25], for the purpose of transforming the electric grid using renewable energy sources to rapidly charge electric vehicles, an inverter for charging electric vehicles with an efficiency similar to that of a drive converter is proposed as a new solution for charging electric vehicle batteries. In [26], an unlimited series input boost converter with high fault tolerance is proposed for vehicle-to-aid applications. Comparative experimental results with series boost converters show that the proposed converter has the best closed-loop performance for a given number of devices.

In summary, hybrid topologies constructed with basic DC/DC converters combine with switched inductors or switched capacitors and, although this can combine the advantages of different independent topologies, the disadvantages of the corresponding independent topologies are also significant. Cascade structures connect more than two topologies to obtain a higher boost ratio in series, but the cost of the converter rises greatly. Z-source (quasi-Z-source) converters can significantly improve the voltage gain of the DC/DC converter, but there is usually a problem in terms of the input and output not connecting on common ground. The effect of input voltage disturbance on the system was also neglected in the study of the above control strategy. Therefore, this paper proposes the topology of

a double-boost converter, and designs a double closed-loop controller to aim for both the feedforward of input voltage disturbance and the feedback of the inductor current to improve the above issues.

## 2. Topology and Operating Principle of the Proposed Converter

### 2.1. Topology of Double-Boost Converter

The proposed double-boost converter is shown in Figure 1. The converter consists of two power switches  $Q_1$ ,  $Q_2$ , two inductors  $L_1$ ,  $L_2$ , three diodes  $D_1$ ,  $D_2$ ,  $D_3$  and an output filter capacitor  $C_1$ . Assuming that the inductors  $L_1$ ,  $L_2$  are the same, the remaining diodes and metal-oxide-semiconductor field-effect transistor (MOSFET) switching also have the same parameters. The two switches in the converter are turned on or off together, and the two operating modes are shown in Figure 2.

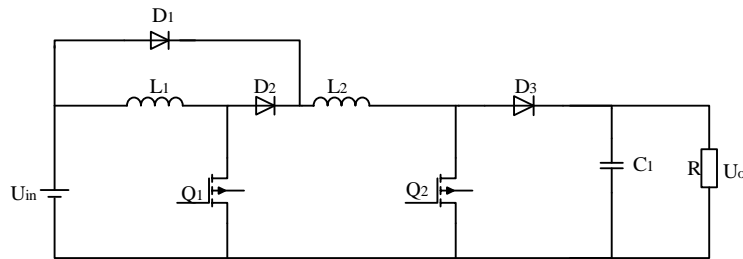


Figure 1. Double-boost converter topology.

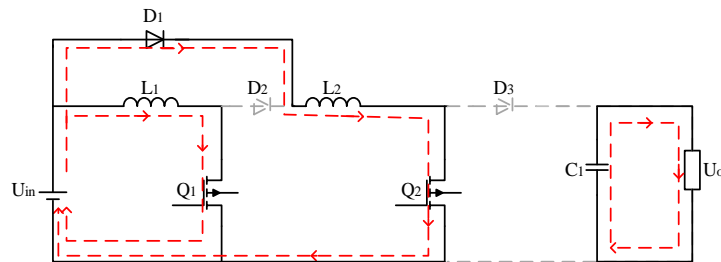


Figure 2. Converter operating mode in ON state.

When switches  $Q_1$  and  $Q_2$  are turned on, that is, the converter is in the ON operating mode, the inductors  $L_1$  and  $L_2$  are charged by the input power source, and the inductors absorb energy; the capacitor  $C_1$  supplies energy to the load. The operating mode of the proposed converter is shown in Figure 2.

In this mode, diode  $D_1$  is turned on, and diodes  $D_2$  and  $D_3$  are turned off under reverse voltage. During this stage, there are three loops in the equivalent circuit. The input power  $U_{in}$  charges the inductor  $L_1$  through the switch  $Q_1$  to form the first loop. The input power  $U_{in}$  charges the inductor  $L_2$  through the switch  $Q_2$  to form the second loop. The output capacitor  $C_1$  provides energy to the load to form the third loop. The voltages across the two inductors  $L_1$  and  $L_2$  are the voltages  $U_{in}$  of the input voltage power source. The voltage and current on the inductor take the associated reference direction, and set  $T_s$  as a Pulse-width modulation (PWM) period,  $D$  is the duty cycle of PWM, then the turn-on time of switches  $Q_1$  and  $Q_2$  is  $D \times T_s$  in one cycle. Suppose that the currents through the inductors  $L_1$  and  $L_2$  are  $I_{L1}$  and  $I_{L2}$ , respectively. In this stage, the currents of the two inductors are equal, and the energy absorbed by the two inductors in a PWM period is shown in Equation (1).

$$W_L = U_{in} \times I_L \times D \times T_s \tag{1}$$

where  $W_L$  represents the energy absorbed by the inductor during the turn-on period of the switch.

When the switches  $Q_1$  and  $Q_2$  are turned off, that is, the equivalent circuit is in the OFF mode, the inductors  $L_1$  and  $L_2$  are connected in series with the input power source to provide energy to the load and charge the capacitor  $C_1$ ; the operating mode of the converter is shown in Figure 3.

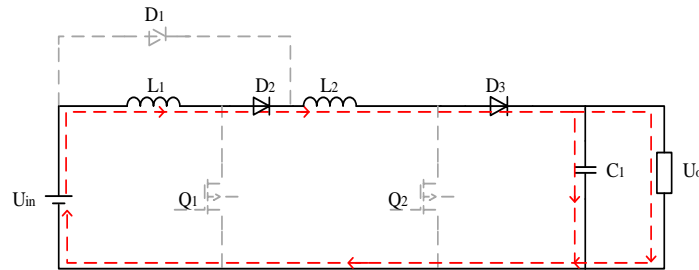


Figure 3. Converter operating mode in OFF state.

In this mode, diodes  $D_2$  and  $D_3$  are turned on, and diode  $D_1$  is turned off under reverse voltage. During this stage, there is only one loop in the equivalent circuit. The input power source  $U_{in}$  and inductors  $L_1$  and  $L_2$  are connected in series to provide energy to the load and charge the output capacitor  $C_1$ . By ignoring the conduction voltage drop in the diode, the voltage across the two inductors  $L_1$  and  $L_2$  are the voltage  $U_{in}$  of the input voltage. The voltage and current reference directions on the inductor are uncorrelated, and the energy released by the two inductors in a PWM period is shown in Equation (2).

$$W'_L = \left( \frac{U_o - U_{in}}{2} \right) \times I_L \times (1 - D) \times T_S \tag{2}$$

where  $1 - D$  represents the turn-off period of the switch, and  $W'_L$  represents the energy released by the inductor during the turn-off period of the switch.

Based on the law of the conservation of energy, the following equation can be obtained as Equation (3).

$$W_L = W'_L \tag{3}$$

According to Equations (1)–(3), the voltage gain  $G_D$  of the proposed converter can be obtained as shown in Equation (4).

$$G_D = \frac{1 + D}{1 - D} \tag{4}$$

By calculating this, the relationship between the voltage gain and the duty cycle  $D$  of the proposed double-boost converter can be obtained, as shown in Figure 4.

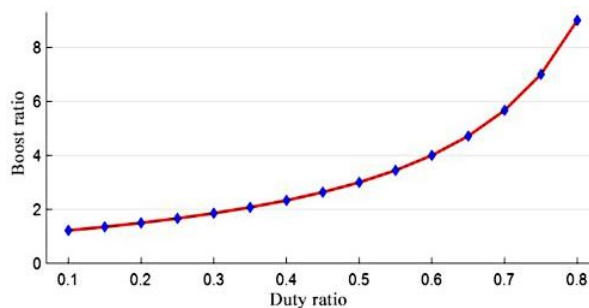


Figure 4. The relationship between voltage gain and duty cycle.

According to the two operating modes and Kirchhoff’s Current Law (KCL), we can obtain the current stress of each device of the proposed converter. In the two operating modes, the capacitor current is represented by  $I_{Con}$  and  $I_{Coff}$ , and the equation is as follows.

$$I_{Con} = -I_o \tag{5}$$

$$I_{Coff} = I_{D3} - I_o \quad (6)$$

where  $I_o$  represents the output current and  $I_{D3}$  represents the current flowing through diode  $D_3$ . By applying ampere-second balance to the capacitor, the following equation can be obtained as

$$I_o \cdot D = (I_{D3} - I_o) \cdot (1 - D) \quad (7)$$

According to Equation (7), the current stress of diode  $D_3$  can be expressed as:

$$I_{D3} = \frac{I_o}{1 - D} \quad (8)$$

Ignoring the loss of the converter, assuming that the input power and the output power are the same, the following equation can be obtained as:

$$U_{in} \cdot I_{in} = U_o \cdot I_o \quad (9)$$

From (4) and (9), the relationship between input current  $I_{in}$  and output current  $I_o$  can be expressed as follows:

$$I_{in} = \frac{1 + D}{1 - D} \cdot I_o \quad (10)$$

According to the operating principle of the ON mode, the current stress of the switches  $Q_1$ ,  $Q_2$  and the diode  $D_1$  can be obtained as:

$$I_{Q1} = I_{Q2} = I_{D1} = \frac{I_{in}}{2} = \frac{1 + D}{2(1 - D)} \cdot I_o \quad (11)$$

where  $I_{Q1}$  and  $I_{Q2}$  represent the current flowing through switches  $Q_1$  and  $Q_2$ , respectively, and  $I_{D1}$  represents the current flowing through the diode  $D_1$ .

According to the operating principle of the OFF mode, the current flowing through the diode  $D_2$  is equal to that of diode  $D_3$ , and it can be described as follows:

$$I_{D2} = I_{D3} = \frac{I_o}{1 - D} \quad (12)$$

Finally, according to Equations (5) and (6) and the root mean square principle of the capacitor current, the current stress  $I_{C1}$  of capacitor  $C_1$  can be obtained as:

$$I_{C1} = \sqrt{\frac{D}{1 - D}} I_o \quad (13)$$

The current stresses of each component in the proposed double-boost converter are shown in Table 1.

**Table 1.** Current stress of each component.

Device Name.	Current Stress
Diode $D_1$	$I_o(1 + D)/2(1 - D)$
Diode $D_2$	$I_o/(1 - D)$
Diode $D_3$	$I_o/(1 - D)$
Switch device $Q_1$	$I_o(1 + D)/2(1 - D)$
Switch device $Q_2$	$I_o(1 + D)/2(1 - D)$
Output capacitor $C_1$	$I_o[D/(1 - D)]^{1/2}$

In order to compare the advantages and disadvantages of several topologies, this paper compares the number of switches, inductors, capacitors and diodes, the theoretical voltage gain, and the voltage

stress on the switch device, the inductor and capacitor, provided that the power grade and input and output voltages of the three topologies are the same. The comparison results are shown in Table 2. The topology of the four-phase interleaved converter is shown in Figure 5.

**Table 2.** Comparison of the proposed converter and other converters.

Converter	Traditional Boost	Four-Phase Interleaving	Double-Boost
Number of inductors	1	4	2
Number of capacitors	1	2	1
Number of switch devices	1	4	2
Number of diodes	1	4	3
Total number of devices	4	14	8
Stress of switch devices	$U_o$	$(U_o + U_{in})/2$	$(U_o + U_{in})/2$
Capacitance	$I_{out}D/(\Delta U \times f)$	$I_{out}D/2(\Delta U \times f)$	$I_{out}D/(\Delta U \times f)$
Inductance	$U_{in}D/(\Delta I_L \times f)$	$U_{in}D/4(\Delta I_L \times f)$	$U_{in}D/2(\Delta I_L \times f)$
Theoretical voltage gain	$1/(1 - D)$	$(1 + D)/(1 - D)$	$(1 + D)/(1 - D)$

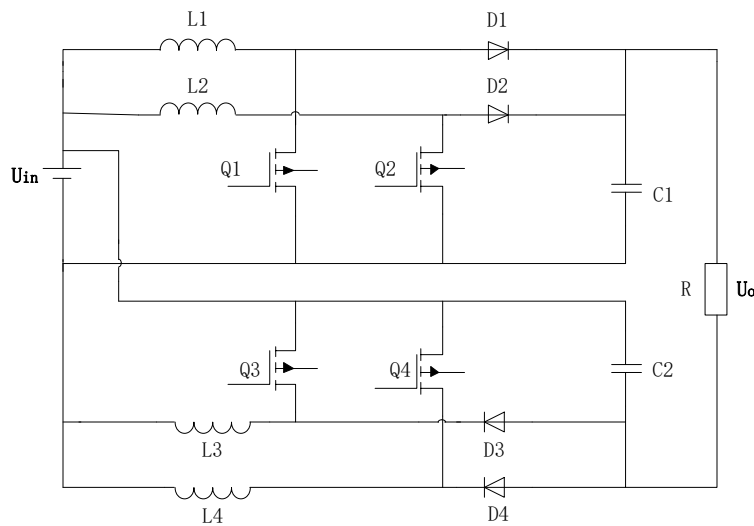


**Figure 5.** Four-phase interleaved converter.

In Table 2,  $\Delta I_L$  is the inductor current ripple,  $\Delta U$  is the output voltage ripple,  $f$  is the switching frequency, and  $D$  is the duty cycle of the PWM. It can be seen from Table 2 that, although the boost converter has the least number of devices, the stress of the switch device is the largest of the three converters. The performance requirements of the switch device are the highest, and the values of inductance and capacitance are the largest, resulting in the power module cost being high, and it is difficult to meet the requirements of high voltage gain in the DC/DC converter. Although the four-phase interleaved DC/DC converter has low stress on the switch device and the smallest value of inductance and capacitance, the converter adopted many devices, resulting in a higher cost. Although the proposed double-boost converter is simple, the number of devices is small, the voltage stress is low when the voltage gain is the same, and the two switches only need the same PWM signal for control.

### 2.2. Operating Principle of Double-Boost Converter

In order to analyze the operating principle of the DC/DC converter in detail, this paper presents its corresponding state equations for different modes. In the process of establishing the state equation, the influence of inductor current fluctuation and capacitor voltage fluctuation on the circuit is considered. The corresponding waveform of the proposed converter in different modes is shown in Figure 6.

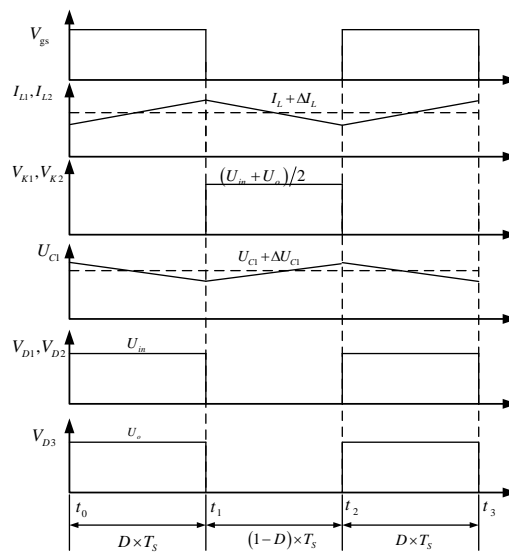


Figure 6. Double-boost converter working waveform.

It can be seen from Figure 6 that, during the  $t_0-t_1$  stage, the switches  $Q_1$  and  $Q_2$  are turned on, and the diodes  $D_2$  and  $D_3$  are turned off due to the reverse voltage. Meanwhile, the input power source  $U_{in}$  charges the inductors  $L_1$  and  $L_2$ , and the inductor current rises linearly. The energy required by the load is provided by the output filter capacitor  $C_1$ , and the capacitor is in a discharged state; therefore, and the capacitor voltage  $U_{C1}$  decreases. Since the parameters of the inductors  $L_1$  and  $L_2$  are the same, take the inductor  $L_1$  as an example for analysis. In this stage, the expression of the inductor current is shown in Equation (14).

$$U_{in} = L_1 \cdot \frac{dI_{L1}}{dt} \tag{14}$$

where  $dI_{L1}$  is the  $\Delta I_L$ ,  $dt = D/f$ ,  $f$  is the switching frequency. The expression of the voltage change in the capacitor  $C_1$  is shown in Equation (15).

$$-\frac{U_{C1}}{R} = C_1 \cdot \frac{dU_{C1}}{dt} \tag{15}$$

where  $dU_{C1} = \Delta U_{C1}$ ,  $\Delta U_{C1}$  is the capacitor voltage fluctuation. From Equations (14)–(16) can be written as:

$$\begin{bmatrix} \frac{dI_{L1}}{dt} \\ \frac{dU_{C1}}{dt} \end{bmatrix} = \begin{bmatrix} 0 & 0 \\ 0 & -\frac{2}{RC_1} \end{bmatrix} \cdot \begin{bmatrix} I_{L1} \\ U_{C1} \end{bmatrix} + \begin{bmatrix} \frac{1}{L_1} \\ \frac{1}{RC_1} \end{bmatrix} \cdot U_{in}, \tag{16}$$

During the  $t_1-t_2$  stage, the switches  $Q_1$  and  $Q_2$  are turned off, and the diode  $D_1$  is turned off due to the reverse voltage, and the inductors  $L_1$  and  $L_2$  are connected in series with the power supply to provide energy to the load and charge capacitor  $C_1$ . Therefore, the inductor current is linearly decreasing and the capacitor voltage is increasing. The expression of the inductor current is shown in Equation (17).

$$L_1 \frac{dI_{L1}}{dt} = \frac{U_{in} - U_{C1}}{2} \tag{17}$$

The expression of the voltage of the capacitor  $C_1$  is shown in Equation (18):

$$C_1 \frac{dU_{C1}}{dt} = I_{L1} - \frac{U_{C1}}{R} \tag{18}$$

According to Equations (17) and (18), the state equation during this stage can be obtained as follows:

$$\begin{bmatrix} \frac{dI_{L1}}{dt} \\ \frac{dU_{C1}}{dt} \end{bmatrix} = \begin{bmatrix} 0 & -\frac{1}{2L_1} \\ \frac{1}{C_1} & -\frac{2}{RC_1} \end{bmatrix} \cdot \begin{bmatrix} I_{L1} \\ U_{C1} \end{bmatrix} + \begin{bmatrix} \frac{1}{2L_1} \\ \frac{1}{RC_1} \end{bmatrix} \cdot U_{in} \tag{19}$$

### 3. Modeling of Double-Boost Converter

When designing and analyzing a DC/DC converter, especially when analyzing its stability and dynamic performance, it is of great significance to use the state space averaging method to establish a small-signal model. The proposed double-boost converter is a non-linear, time-varying system, which can be regarded as a state space that approximates the first-order averaging method. Thus, the method can be used to translate the variables of the converter system into an average quantity over a period of time. It consists of a DC steady-state component and an AC small-signal component. After calculation, the AC small-signal quantity and the DC steady-state quantity are separated, the small signal is linearized and, finally, the DC of the double-boost converter can be obtained for the steady-state model and AC small signal model.

When the switches  $Q_1$  and  $Q_2$  are turned on, the corresponding state equation of the converter in this mode is expressed by Equation (16). When the switches  $Q_1$  and  $Q_2$  are turned off, the corresponding state equation of the converter in this mode is expressed by Equation (19).

In a PWM period, the state space average method can be obtained by averaging the various quantities of the converter using the state space averaging method, as shown in Equation (20).

$$\begin{bmatrix} \frac{d\bar{I}_{L1}}{dt} \\ \frac{d\bar{U}_{C1}}{dt} \end{bmatrix} = \begin{bmatrix} 0 & -\frac{1-\bar{D}}{2L_1} \\ \frac{1-\bar{D}}{C_1} & -\frac{2}{RC_1} \end{bmatrix} \cdot \begin{bmatrix} \bar{I}_{L1} \\ \bar{U}_{C1} \end{bmatrix} + \begin{bmatrix} \frac{1+\bar{D}}{2L_1} \\ \frac{1}{RC_1} \end{bmatrix} \cdot \bar{U}_{in} \quad (20)$$

Among them,  $\bar{D}$ ,  $\bar{I}_{L1}$ ,  $\bar{U}_{C1}$  and  $\bar{E}$  are the average value of the duty cycle, inductor current, input voltage and output voltage in a cycle, respectively. When the average value of the duty ratio  $\bar{D} = 1$ , the state space average equation is the state equation when the switch is turned on. When the average value of the duty cycle  $\bar{D} = 0$ , the state space average equation is the state equation when the switch is turned off. As mentioned above, the average quantity obtained by the state space averaging method can be expressed as the form of the addition of the DC steady-state quantity and the AC small-signal quantity, as shown in Equation (21).

$$\begin{cases} \bar{D} = D + \hat{D} \\ \bar{I}_{L1} = I_{L1} + \hat{I}_{L1} \\ \bar{U}_{C1} = U_{C1} + \hat{U}_{C1} \\ \bar{U}_{in} = U_{in} + \hat{U}_{in} \end{cases} \quad (21)$$

Among them,  $D$ ,  $U_{C1}$  and  $U_{in}$ , are the DC steady-state quantities, and  $\hat{D}$ ,  $\hat{U}_{C1}$ ,  $\hat{E}$  and  $\hat{I}_{L1}$  are the AC small-signal components of variables. By taking Equation (21) into (20), and using the average quantity in the state space average equation with Equation (21), the following equation can be obtained:

$$\begin{bmatrix} \frac{d(I_{L1} + \hat{I}_{L1})}{dt} \\ \frac{d(U_{C1} + \hat{U}_{C1})}{dt} \end{bmatrix} = \begin{bmatrix} 0 & -\frac{1-(D+\hat{D})}{2L_1} \\ \frac{1-(D+\hat{D})}{C_1} & -\frac{2}{RC_1} \end{bmatrix} \cdot \begin{bmatrix} I_{L1} + \hat{I}_{L1} \\ U_{C1} + \hat{U}_{C1} \end{bmatrix} + \begin{bmatrix} \frac{1+(D+\hat{D})}{2L_1} \\ \frac{1}{RC_1} \end{bmatrix} \cdot (U_{in} + \hat{U}_{in}) \quad (22)$$

By ignoring the second-order infinitesimal, the DC steady-state quantity and the AC small-signal quantity are separated, and the DC steady-state model of the double-boost converter can be obtained as:

$$\begin{bmatrix} U_{C1} \\ I_{L1} \end{bmatrix} = \begin{bmatrix} \frac{1+D}{1-D} U_{in} \\ \frac{U_{C1}}{R(1-D)} \end{bmatrix} \quad (23)$$

It can be seen from the DC steady-state model, the voltage gain of double-boost converter is  $1 + D/1 - D$ , it is consistent with the result of voltage gain obtained by the law of energy conservation. In addition, the obtained AC small-signal model of the dual-boost converter can be written as follows:

$$\begin{bmatrix} \frac{d\hat{I}_{L1}}{dt} \\ \frac{d\hat{U}_{C1}}{dt} \end{bmatrix} = \begin{bmatrix} 0 & -\frac{1-D}{2L_1} \\ \frac{1-D}{C_1} & -\frac{2}{RC_1} \end{bmatrix} \cdot \begin{bmatrix} \hat{I}_{L1} \\ \hat{U}_{C1} \end{bmatrix} + \begin{bmatrix} \frac{1+D}{2L_1} \\ \frac{1}{RC_1} \end{bmatrix} \cdot \hat{U}_{in} + \begin{bmatrix} \frac{U_{C1}+U_{in}}{2L_1} \\ -\frac{\hat{I}_{L1}}{C_1} \end{bmatrix} \cdot \hat{D} \quad (24)$$

The small-signal model of the dual-boost converter is transformed into the s domain by Laplace transform:

$$\hat{U}_C(s) = \frac{R(1-D)[R(1-D^2)+2Ls]}{[R(1-D^2)+2Ls](RCs+2)-2RLCs^2-4Ls-R(1-D)^2} \hat{I}_{L1}(s) + \frac{R(1-D)(U_C+U_{in})-2I_{L1}RLs-RI_{L1}[R(1-D^2)+2Ls]}{[R(1-D^2)+2Ls](RCs+2)-2RLCs^2-4Ls-R(1-D)^2} \hat{D}(s) \quad (25)$$

$$\hat{I}_{L1}(s) = \frac{2L_1RL(1-D)+2RLCs(U_C+U_{in})+4L(U_C+U_{in})}{2L[2RLCs^2+4Ls+R(1-D)^2]} \hat{D}(s) + \frac{2L(1-D)+2RLCs(1+D)+4L(1+D)}{2L[2RLCs^2+4Ls+R(1-D)^2]} \hat{U}_{in}(s) \quad (26)$$

From Equations (25)–(27) can be expressed as:

$$\hat{U}_C(s) = \frac{R(1-D)(U_C+U_{in})+2RLs \cdot I_{L1}}{2L_1C_1R \cdot s^2+4L_1 \cdot s+(1-D)^2R} \hat{D}(s) + \frac{R(1-D^2)+2Ls}{2L_1C_1R \cdot s^2+4L_1 \cdot s+(1-D)^2R} \hat{U}_{in}(s) \quad (27)$$

According to Equations (25)–(27), the transfer function of the duty cycle  $D$  to the inductor current  $I_{L1}$  can be obtained as:

$$G_{D \rightarrow I_{L1}}(s) = \frac{2RLI_{L1}(1-D) + 2RLCs(U_C + U_{in}) + 4L(U_C + U_{in})}{2L[2RLCs^2 + 4Ls + R(1-D)^2]} \quad (28)$$

Meanwhile, according to Equations (25)–(27), the transfer function from the input voltage to the inductor current can be written as:

$$G_{U_{in} \rightarrow I_{L1}}(s) = \frac{2L(1-D) + 2RLCs(1+D) + 4L(1+D)}{2L[2RLCs^2 + 4Ls + R(1-D)^2]} \quad (29)$$

Similarly, the transfer function of the inductor current  $I_{L1}$  to output voltage  $U_o$  is shown in Equation (30).

$$G_{I_{L1} \rightarrow U_{C1}}(s) = \frac{R(1-D)[R(1-D^2)+2Ls]}{[R(1-D^2)+2Ls](RCs+2)-RLCs^2-4Ls-R(1-D)^2} \quad (30)$$

The transfer function  $G_{D \rightarrow U_{C1}}(s)$  of duty cycle  $D$  to the output voltage is shown in Equation (31).

$$G_{D \rightarrow U_{C1}}(s) = \frac{R(1-D)(U_C + U_{in}) + 2RL \cdot s \cdot I_{L1}}{2L_1C_1R \cdot s^2 + 4L_1 \cdot s + (1-D)^2R} \quad (31)$$

According to the above transfer function, the output voltage, the inductor current double closed-loop system is shown in Figure 7.

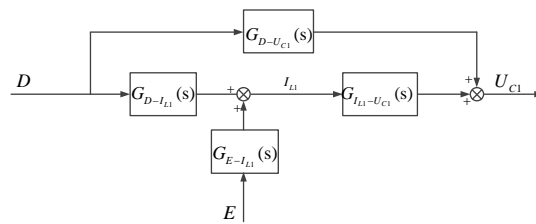


Figure 7. Small signal model.

#### 4. Design of the Double-Boost Converter Controller

##### 4.1. Calculation of Inductor and Capacitor of Converter

The parameters of the experimental prototype are as follows: the input voltage is 20 V, the rated output voltage is 100 V, the rated load is 100  $\Omega$ , the output power rating is 100 W, the values of inductors  $L_1$  and  $L_2$  are both 0.35 mH, the value of the capacitor is 47  $\mu\text{F}$ , the type of switch is IFR640N, the type of diode is DFE10I600PM and the switching frequency is 20 kHz [21].

According to Equation (32), the inductance value can be calculated as:

$$L_1 = L_2 = \frac{U_{in} \times D}{2 \times \Delta I_L \times f} \quad (32)$$

where  $\Delta I_L$  is the inductor current ripple; taking 20% of the average current as the inductor current ripple, the inductance value of the two inductors can be calculated to be 0.35 mH.

According to Equation (33), the capacitance value can be calculated as:

$$C_1 = \frac{I_{out} \times D}{\Delta U \times f} = 35 \mu\text{F} \quad (33)$$

where  $\Delta U$  is the output voltage fluctuation, taking 1% of the average output voltage as the capacitor voltage fluctuation, and the capacitor value can be calculated as 47  $\mu\text{F}$ .

##### 4.2. Design of Feedforward Double Closed-Loop Feedback Controller

In order to design the controller of the dual-boost converter, the algebraic expression of the transfer function needs to be obtained. By substituting the obtained inductance, capacitance and other parameters into Equation (31), the following equation can be obtained as

$$G_{D-U_{C1}}(s) = \frac{-0.75s + 4000}{7 \times 10^{-2} \times s^2 + 1.4 \times 10^{-3} \times s + 11.11} \quad (34)$$

Similarly, transfer function of the duty cycle  $D$  to the inductor current and the transfer  $G_{I_{L1}-U_{C1}}(s)$  function of the inductor current to the output voltage can expressed as:

$$G_{D-I_{L1}} = \frac{3.95 \times 10^{-4}s + 0.226}{2.3 \times 10^{-9}s^2 + 0.98 \times 10^{-6}s + 11.11} \quad (35)$$

$$G_{I_{L1}-U_{C1}}(s) = \frac{2.33 \times 10^{-2}s + 1851.15}{1.65 \times 10^{-6}s^2 + 0.26s + 100} \quad (36)$$

According to Equations (35) and (36), a double closed-loop PI controller based on output voltage and inductor current is designed, and the control functions  $G_{C1}(s)$  and  $G_{C2}(s)$  adopt PI control. The control block diagram is shown in Figure 8 and is achieved by the following steps: setting the reference voltage  $U_{ref}$ ; comparing the output voltage value  $U_{C1}$  with the reference voltage to get error signal  $e_1$ ; sending the signal to the PI controller  $G_{C1}(s)$  to obtain the reference current  $I_{L1'}$ ; comparing this with the actual inductor current to get error signal  $e_2$ ; then, the adjusted duty ratio  $D$  can be

obtained through the PI controller  $G_{C2}(s)$ . Meanwhile, the adjusted output voltage is obtained through the transfer functions  $G_{D-I_{L1}}(s)$  and  $G_{I_{L1}-U_{C1}}(s)$ .

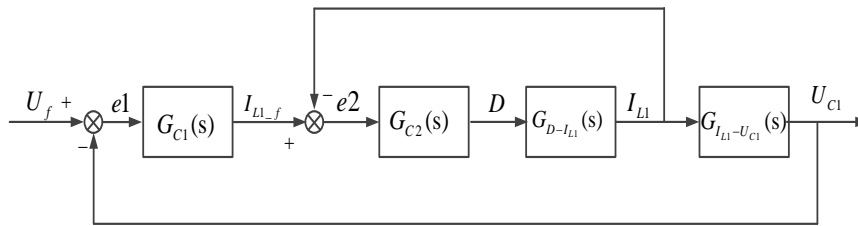


Figure 8. Double closed-loop control system.

As shown in Figure 7, the input voltage will also have a certain impact on the output of the system; considering fluctuations in the output voltage, the control block diagram of the system is shown in Figure 8.

From Figure 9, it is clear that once the input voltage of the DC/DC converter fluctuates, it will affect the value of the inductor current, which, in turn, affects the output voltage of the system. Therefore, in order to eliminate the influence of input voltage fluctuation on the output voltage of the system, it is necessary to introduce a feedforward loop from the input voltage to the inductor current. The gain of this feedforward loop is the negative value of the input voltage to the inductor current transfer function  $G_{E \rightarrow I_{L1}}(s)$ ; the control block diagram is shown in Figure 10.

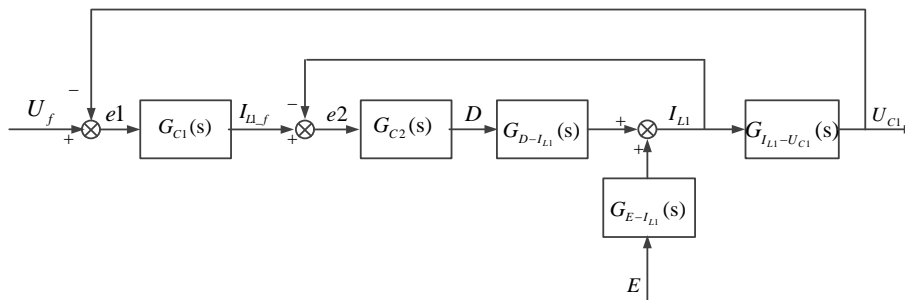


Figure 9. Control block diagram after adding input voltage disturbance.

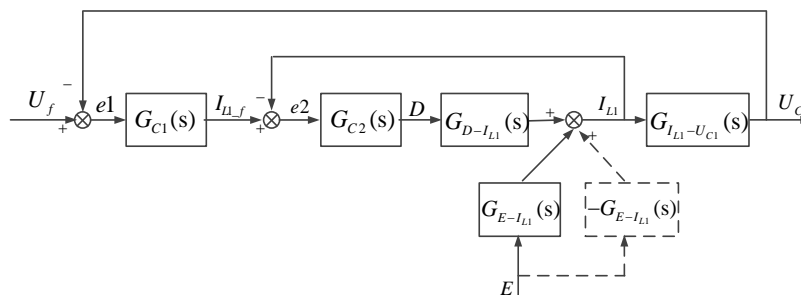


Figure 10. Control block diagram after the introduction of input voltage feedforward control.

As shown in Figure 10, adding feedforward cancels the effect of input voltage fluctuation on the inductor current, but, in the actual circuit, the output voltage can only be controlled by the duty cycle. Therefore, the feedforward control acting on the inductor current is equivalent to the feedforward control acting on the duty cycle  $D$ . The equivalent control block diagram is shown in Figure 11.

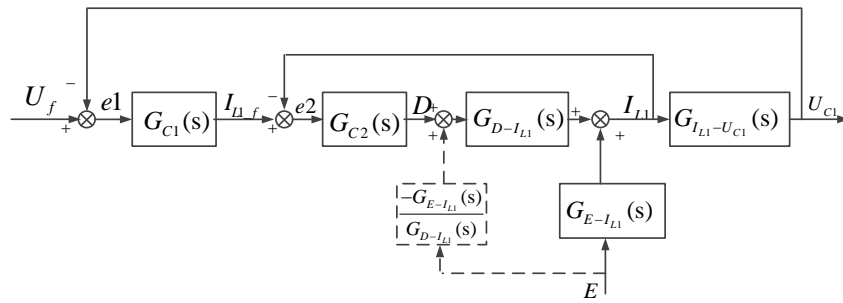


Figure 11. Block diagram of equivalent feedforward control.

Figure 11 shows the relationship between the transfer function of feedforward control and the duty cycle to the transfer function of the inductance current, expressed as  $G_f(s)$ . According to Equations (28) and (29), the transfer function of feedforward control can be expressed as:

$$G_f(s) = -\frac{2L(1 - D) + 2RLCs(1 + D) + 4L(1 + D)}{2RL_{L1}(1 - D) + 2RLCs(U_{C1} + U_{in}) + 4L(U_{C1} + U_{in})} \tag{37}$$

### 5. Simulation and Experimental Results Analysis

#### 5.1. Simulation Results and Analysis

In order to verify the rationality of the proposed converter, a simulation model of the converter is established in this paper and the simulation parameters are shown in Table 3.

Table 3. Design parameters of the converter.

Parameters	Values
Rated power $P$	100 W
Input voltage $U_{in}$	20 V
Rated output Voltage $U_O$	100 V
Rated load resistance $R_L$	100 $\Omega$
Switching frequency $f$	20 kHz
Inductor $L_1$ and $L_2$	0.35 mH
Capacitor	47 $\mu$ F
Power switches	IFR640N
Diodes	DFE10I600PM

The simulation result when the input voltage is 20 V and the output reference voltage is 100 V is shown in Figure 12. From Figure 12: the output voltage is stable at 100 V; the inductor current linearly increases when the switch is turned on, and linearly decreases when the switch is turned off; there is no inductor current discontinuity, which is consistent with the previous theoretical calculation. From the simulation results, it can be seen that, when the driving signal  $V_{gs}$  is about 0.67, the output voltage of the proposed converter is 100 V, and a higher voltage gain can be obtained without using the extreme duty cycle, which proves the effectiveness of the proposed converter.

To further illustrate the advantages of the proposed converter in terms of voltage gain, the voltage gain curves of the proposed converter are compared with those of conventional boost converters and several other converters, as shown in Figure 13. Compared to conventional boost converters, the proposed converters have a higher boost ratio at non-limiting duty cycles. Although the boost ratios of the converters in [18] and [27] are higher, the input and output sides of these converters are non-commonly connected, which limits their practical application. The proposed converter has the same voltage gain as the one in [28], but, similar to the previous two converters, its input and output sides are non-commonly connected. Therefore, in summary, the proposed converters not only have a higher boost ratio, but are also more suitable for practical engineering applications.

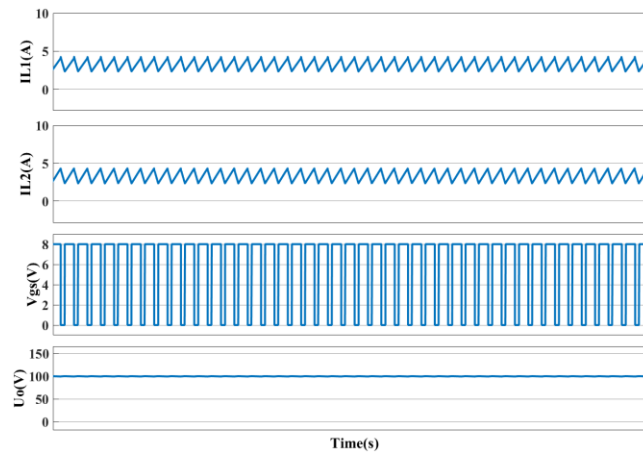


Figure 12. Simulation results of converter.

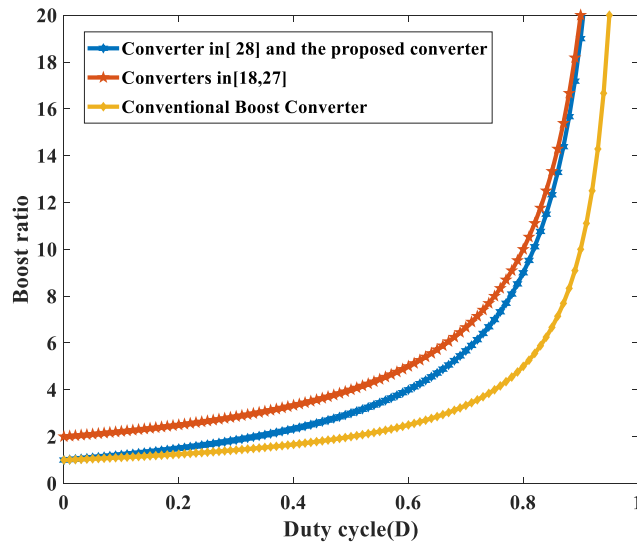
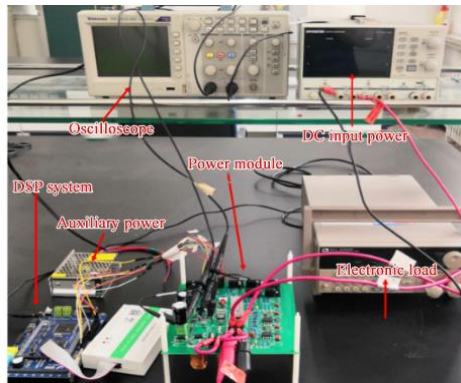


Figure 13. Comparison of boost ratio curves for different converters.

5.2. Experimental Platform Construction

In order to verify the effectiveness of the proposed converter and control method, an experimental platform was designed, as shown in Figure 14a. The experimental platform includes a DC power supply, oscilloscope, electronic load, a DSP28335 controller and an experimental prototype. The experimental prototype includes the proposed converter, drive circuit, voltage detection circuit, current detection circuit and auxiliary power circuit. In addition, we compare the proposed converter with the four-phase interleaved experimental prototypes made before, as shown in Figure 14b. In order to facilitate the comparison of the various indicators of the proposed double-boost converter, the voltage gain in the open-loop state of the proposed double-boost converter was measured first. Under the same experimental conditions, when comparing the proposed converter with the four phase interleaved DC/DC converter and the traditional boost converter, the input voltage is 20 V, the output voltage is 100 V, the load is 100 Ω, and the switching frequency of the system is 20 kHz, as shown in Table 3, thus verifying the effectiveness of the proposed double-boost converter controller. Finally, the efficiency of the proposed converter is measured under the conditions of variable load, variable frequency and variable output voltage. Compared with the four-phase interleaved DC/DC converter and traditional boost converter, the advantages of the proposed dual-boost converter are highlighted.



(a)



(b)

**Figure 14.** The prototype of proposed converter. (a) The experimental platform of double-boost converter. (b) Experimental prototype of four-phase interleaved DC/DC converter.

5.3. Function Test of the Prototype

In the open loop state, the duty cycle is in the range of 0.2–0.8, and the actual boost ratio of the proposed dual-boost converter was tested, and compared with the four-phase interleaved DC/DC converter and traditional boost converter. The experimental results of the three converters are shown in Figure 15.

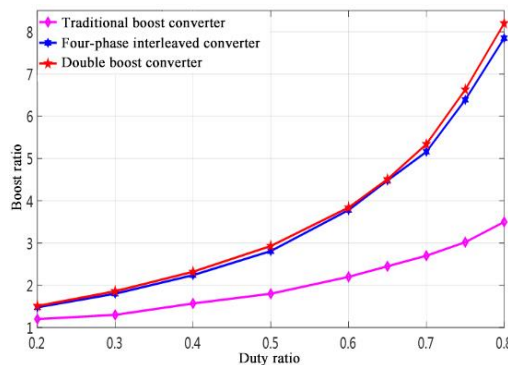


**Figure 15.** Comparison curve of measured boost ratio.

From Figure 15, it can be seen that, compared with the traditional boost converter, the proposed double-boost converter has obvious advantages. In the traditional boost converter, when the duty ratio is 0.2, the actual voltage gain is 1.21 times, and when the duty ratio is 0.8, the actual voltage gain is

3.54 times; the proposed double-boost converter has an actual voltage gain ratio of 1.52 times when the duty ratio is 0.2, and an actual voltage gain of 8.21 times when the duty ratio is 0.8. As the duty cycle increases, the difference between the actual voltage gain of the two converters gradually increases.

In order to further reflect the advantages of the proposed converter in terms of voltage gain, the voltage gain improvement curve compared to the traditional converter is drawn in the range of a 0.2–0.8 duty cycle, as shown in Figure 16.

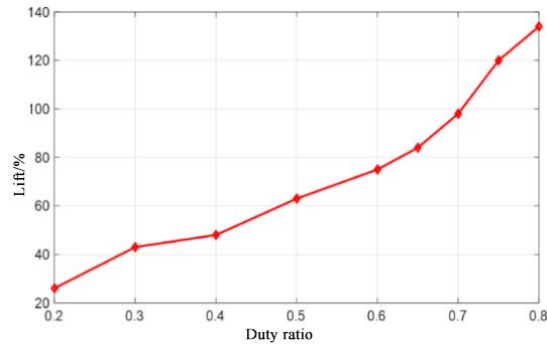


**Figure 16.** Voltage gain improvement curve.

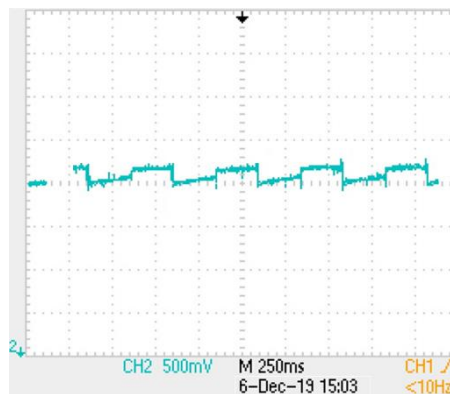
From Figure 16, as the duty cycle  $D$  increases from 0.2, the degree of voltage gain of the proposed double-boost converter relative to the boost converter also increases rapidly. When the duty cycle  $D$  is equal to 0.2, the minimum degree of improvement is 26%, and when the duty cycle  $D$  is equal to 0.8, the degree of improvement can reach 132%.

To verify the feasibility of the proposed double converter application, the output voltage ripple of different converters was measured by setting the input voltage as 6 V and the output voltage as 20 V. The measured results are shown in Figure 17. From Figure 17, the output voltage ripple of the traditional boost converter is the largest, the ripple coefficient reaches 0.015, the output voltage ripple of the four-phase interleaved DC/DC converter is the smallest, the ripple coefficient is 0.0075, and the proposed converter ripple coefficient is 0.01. Although the ripple coefficient is slightly inferior to the four-phase interleaved DC/DC converter, it still has a large advantage in terms of the number of devices, the volume and the control complexity.

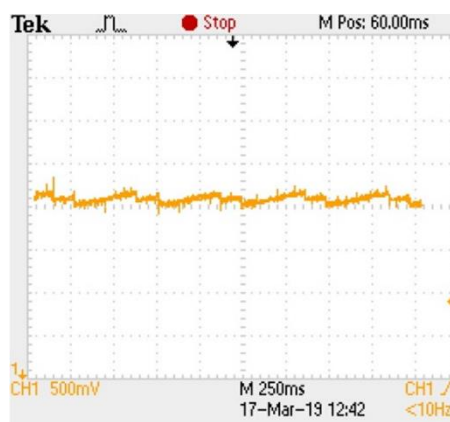


(a)

**Figure 17.** Cont.



(b)

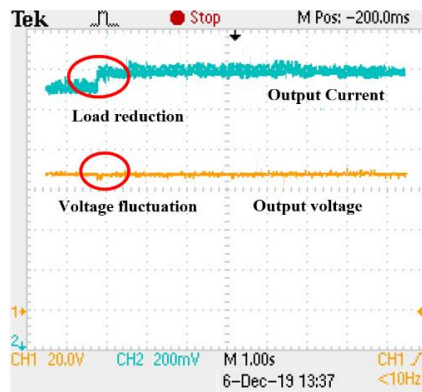


(c)

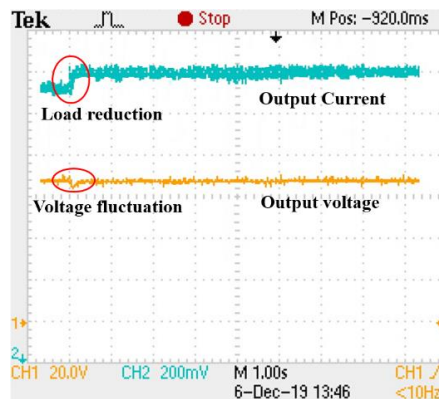
**Figure 17.** Output voltage ripple of three converters. (a) Boost converter. (b) Double-boost converter. (c) Four-phase interleaved DC/DC converter.

#### 5.4. Control Algorithm Verification

In order to verify the robustness of the feedforward–feedback controller designed in this paper, the input was 20 V, the output was 60 V, and the load changed from 100  $\Omega$  to 60  $\Omega$ . The output voltage waveform of the proposed double-boost converter under load disturbance with or without feedforward control is shown in Figure 18. At the moment of load reduction, the output voltage of the control system without feedforward has a fluctuation of about 3 V, and the output voltage fluctuation in the feedforward double closed-loop control system is significantly smaller than that of the control system without feedforward. The experimental results prove that the feedforward double closed-loop control system designed in this paper has good robustness.



(a)



(b)

**Figure 18.** With or without feedforward control effect diagram. (a) Feedforward dual closed-loop control output waveform. (b) Output waveform without feedforward control.

5.5. Efficiency Test of the Prototype

In order to measure the efficiency of the proposed double-boost converter, the input voltage is set to 20 V, the load is 100  $\Omega$ , and the output voltage varies from 30 V to 100 V. Efficiency is measured using a DC regulated power supply and readings from electronic loads. Under this measured condition, the efficiencies of the proposed converter, a traditional boost converter and a four-phase interleaved DC/DC converter are measured and compared. Since the duty cycle varies in the range of 0.2~0.8, the output voltage of boost converter is changed from 30 V to 85 V. The experimental results are shown in Figure 19.

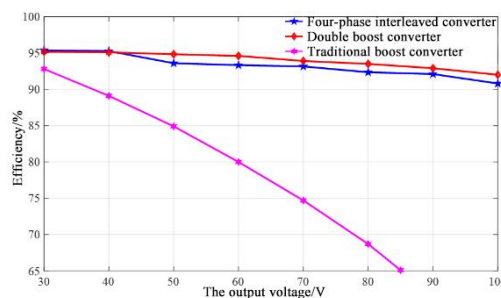


**Figure 19.** Efficiency comparison at different output voltages.

When the load is  $100\ \Omega$ , the switching frequency is determined and it is noted that the three converters have the highest efficiency when the output voltage is the smallest, and the lowest efficiency when the output voltage is the highest, as shown in Figure 19. This phenomenon is because, when the load is constant, the output current decreases with the decrease in the output voltage, so the inductor loss and switching loss are small and the efficiency is high. When the output voltage is 30 V, the efficiency of the proposed double-boost converter and the four-phase interleaved DC/DC converter are similar, both exceeding 95%, but when it exceeds 40 V, the efficiency of the former is significantly higher than the latter. When the load is 100 V, the minimum efficiency of the former is 92%, while the latter is 90.81%. The traditional boost converter has a maximum efficiency of 92.8% and a minimum efficiency of 65.1%, which are significantly different from the previous two converters.

In order to further prove the advantages of the high efficiency of the proposed converter, we set the input voltage to 20 V, the output voltage to 60 V, the switching frequency to 20 kHz, and varied the load from  $50\ \Omega$  to  $100\ \Omega$ . The experimental results are shown in Figure 20. It can be seen from the figure that the order of efficiency of the three converters from high to low is the double-boost converter, the four-phase interleaved DC/DC converter, and the traditional boost converter. The highest efficiencies are 94.6%, 93.59% and 84.9%, respectively, and the lowest efficiencies are 91.42%, 90.16% and 80%, respectively. Therefore, the proposed double-boost converter has obvious advantages in terms of efficiency.

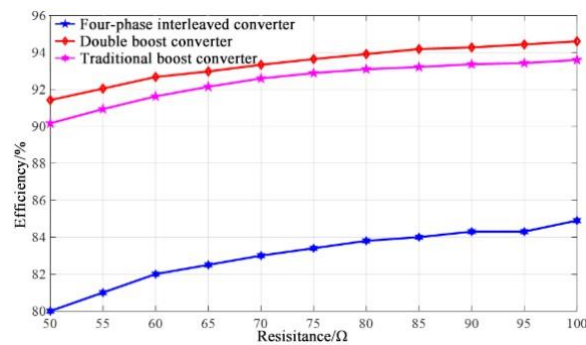
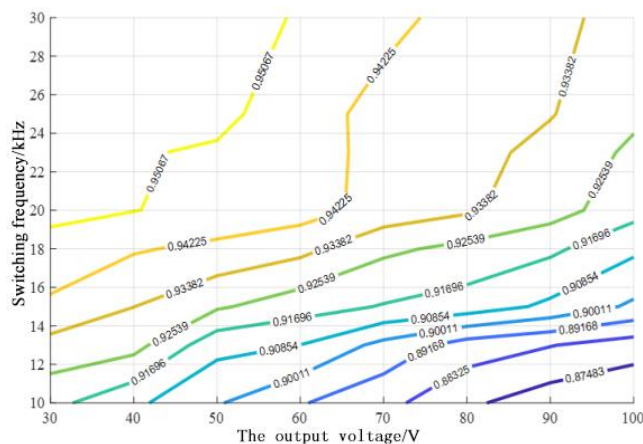


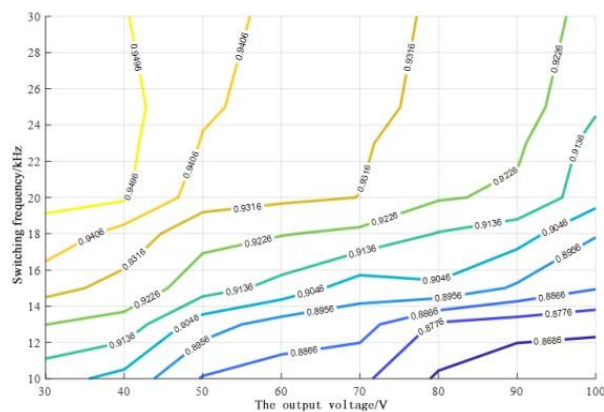
Figure 20. Efficiency comparison under different loads.

Figure 21 shows the efficiency curve of the proposed converter and the four-phase interleaved converter at different switching frequencies; the input voltage is set to 20 V, the load resistance is  $100\ \Omega$ , the frequency is in the range of 10 kHz–30 kHz, and the output voltage is in the range of 30 V–100 V.



(a)

Figure 21. Cont.



(b)

**Figure 21.** Comparison of efficiency of two converters. (a) The efficiency of the proposed converter. (b) Efficiency of four-phase interleaved DC/DC converter efficiency.

As can be seen in Figure 21a, when the switching frequency is constant, as the output voltage increases, the output current gradually increases and the efficiency of the converter decreases due to the increased losses of the converter. When the output voltage is constant, as the switching frequency increases, the efficiency of the converter gradually increases. The maximum efficiency of the proposed converters under this test condition is about 95%. Similarly, the efficiency curves of the four-phase interleaved converter represented in Figure 21b have the same trend as the efficiency curves of the proposed converters in that the efficiency of the converters gradually decreases as the output voltage increases, and the maximum efficiency of the two converters is approximately the same. However, a comparison of Figure 21a,b shows that the efficiency region of more than 90% of the proposed converter is significantly larger than the four-phase interleaved converter, indicating that the proposed converter has a higher efficiency at the same output voltage and frequency. Thus, the proposed converter is more suitable for high voltage gain applications.

## 6. Conclusions

In this paper, a high-gain dual-boost converter for electric vehicles is presented. Through the analysis of the proposed converter operating principle, modeling, controller design, experimental prototype test results, and comparison results with four-phase interleaved DC/DC converters and conventional boost converters commonly used in electric vehicles, the following conclusions can be drawn:

- (1) Considering the voltage gain, device stress, and number of components, the proposed converter has certain advantages over traditional boost converters and four-phase interleaved converters. Compared to four-phase interleaved DC/DC converters, this converter has a simple operating principle and only requires two of the same PWM signals.
- (2) For the double-boost converter, the proposed feedforward double closed-loop control is more robust than the feedforward double closed-loop control; when the load and input voltage change suddenly, it can make the output voltage return to stability faster.
- (3) This can be obtained through the construction of the experimental prototype of the proposed double-boost converter and by comparison with the four-phase interleaved DC/DC converter and the traditional boost converter. In terms of the actual voltage gain and system efficiency under different conditions, the proposed double converter has obvious advantages. The efficiency is measured and compared from three aspects: different output voltages, different loads and different frequencies: In addition, the output voltage ripple of the proposed double-boost converter is smaller than that of the traditional boost converter. Although it is slightly larger than the four-phase interleaved DC/DC converter, the double-boost converter has the advantages

of fewer devices, simple control and high efficiency, making up for the output voltage ripple, which is slightly higher than the four-phase interleaved disadvantages of DC/DC converters.

**Author Contributions:** Project administration, J.D. B.Y. wrote the paper. Z.L. participated in the writing of the paper. All authors have read and agreed to the published version of the manuscript.

**Funding:** This work was supported by the National Key Technologies R&D Program of MOST of China (2018YFB0106300).

**Conflicts of Interest:** The authors declare no conflict of interest.

## Glossary

Electric vehicle	EV
New energy vehicles	NEVs
$D$	Duty cycle of PWM
$T_S$	A PWM period
$W_L$	Energy absorbed by inductor during ON state
$W_L'$	Energy released by inductor during OFF state
$G_D$	Voltage gain
$\Delta I_L$	The inductor current ripple
$\Delta U$	The output voltage ripple
$f$	Switching frequency
$\bar{D}$	Average value of the duty cycle
$\bar{I}_{L1}$	Average value inductor current
$\bar{U}_{C1}$	Average value output voltage
$\bar{E}$	Average value input voltage
$\hat{D}$	AC small-signal component of $D$
$\hat{U}_{C1}$	AC small-signal component of $U_{C1}$
$\hat{E}$	AC small-signal component of $E$
$\hat{I}_{L1}$	AC small-signal component of $I_{L1}$
$G_{D \rightarrow I_{L1}}(s)$	Transfer function of $D$ to the inductor current $I_{L1}$
$G_{U_{in} \rightarrow I_{L1}}(s)$	The transfer function from input voltage to inductor current
$G_{I_{L1} \rightarrow U_{C1}}(s)$	The transfer function of the inductor current $I_{L1}$ to output voltage
$G_{D \rightarrow U_{C1}}(s)$	The transfer function of duty cycle to output voltage
$G_{C1}(s)$	The transfer function of voltage PI controller
$G_{C2}(s)$	The transfer function of current PI controller
$G_f(s)$	The transfer function of feedforward control

## References

- Zachary, C.; Dustin, B.; Siyu, Y.; Andreas, H.; Jun, L.; Michael, F.; Zhongwei, C. Batteries and fuel cells for emerging electric vehicle markets. *Nat. Energy* **2018**, *3*, 279–289.
- Yujie, W.; Zhendong, S.; Zonghai, C. Energy management strategy for battery/supercapacitor/fuel cell hybrid source vehicles based on finite state machine. *Appl. Energy* **2019**, *254*, 113707.
- Wei, G.; Quanming, L.; Yang, Z.; Xingyu, L.; Luowei, Z. A high step-up DC-DC converter with zero input current ripple. *Trans. China Electrotech. Soc.* **2018**, *33*, 284–292.
- Moradisizkoochi, H.; Elsayad, N.; Mohammed, O.A. A family of three-port three-level converter based on asymmetrical bidirectional half-bridge topology for fuel cell electric vehicle applications. *IEEE Trans. Power Electron.* **2019**, *34*, 11706–11724. [[CrossRef](#)]
- García-Vite, P.M.; Rosas-Caro, J.C.; Martínez-Salazar, A.L.; de Jesus Chavez, J.; Valderrábano-González, A.; Sánchez-Huerta, V.M. Quadratic buck-boost converter with reduced input current ripple and wide conversion range. *IET Power Electron.* **2019**, *12*, 3977–3986. [[CrossRef](#)]
- Ali, A.; Hossein, A.; Amir, F. A novel high step-up DC/DC converter based on integrating coupled inductor and switched-capacitor techniques for renewable energy applications. *IEEE Trans. Power Electron.* **2015**, *30*, 4255–4263.
- Milad, B.; Jean-Philippe, M.; Gael, M.; Serge, P.; Mathieu, W.; Farid, M.; Majid, Z. Design and modeling of an equalizer for fuel cell energy management systems. *IEEE Trans. Power Electron.* **2019**, *34*, 10925–10935.

8. Changyong, L.; Jinbin, Z.; Ling, M.; Mingjie, Z.; Yutong, L. A high step-down DC-DC converter. *Trans. China Electrotech. Soc.* **2019**, *34*, 4264–4271.
9. Si, C.; Luowei, Z.; Quanming, L.; Wei, G.; Yuqi, W.; Pengju, S.; Xiong, D. Research on topology of the high step-up boost converter with coupled inductor. *IEEE Trans. Power Electron.* **2019**, *34*, 10733–10745.
10. Hanging, W.; Arnaud, G.; Daniel, H. A review of DC/DC converter-based electrochemical impedance spectroscopy for fuel cell electric vehicles. *Renew. Energy* **2019**, *141*, 124–138.
11. Reza, B.M.; Faeghi, B.H.A. A high efficiency nonisolated buckboost converter based on ZETA converter. *IEEE Trans. Ind. Electron.* **2020**, *67*, 1991–1998.
12. Ilhan, K.; Sude, K.; Naci, G.; Hasan, U. Design and application of PEM fuel cell-based cascade boost converter. *Electr. Eng.* **2019**. [[CrossRef](#)]
13. Qian, L.; Huangfu, Y.; Liangcai, X.; Jiang, W.; Rui, M.; Dongdong, Z.; Fei, G. An improved floating interleaved boost converter with the zero-ripple input current for fuel cell applications. *IEEE Trans. Energy Convers.* **2019**, *34*, 2168–2179.
14. Arab, A.S.; Shokrollahi, M.J. A novel high voltage gain noncoupled inductor SEPIC converter. *IEEE Trans. Ind. Electron.* **2019**, *66*, 7099–7108.
15. Fernao, P.V.; Armando, C.; Daniel, F.; Fenando, S.J. High step-up DC-DC converter for fuel cell vehicles based on merged quadratic boost-cuk. *IEEE Trans. Veh. Technol.* **2019**, *68*, 7521–7530.
16. Banaei, M.R.; Sani, S.G. Analysis and implementation of a new SEPIC-based single switch buck-boost dc-dc converter with continuous input current. *IEEE Trans. Power Electron.* **2018**, *33*, 10317–10325. [[CrossRef](#)]
17. Yun, Z.; Lei, Z.; Mark, S.; Ping, W. Single-Switch, Wide Voltage-Gain Range, Boost DC–DC Converter for Fuel Cell Vehicles. *IEEE Trans. Veh. Technol.* **2018**, *67*, 134–145.
18. Yun, Z.; Heyu, L.; Jing, L.; Mark, S.; Changliang, X. A DC-DC Boost Converter with a Wide Input Range and High Voltage Gain for Fuel Cell Vehicles. *IEEE Trans. Power Electron.* **2018**, *34*, 4100–4111.
19. Shahin, A.; Hinaje, M.; Martin, J.; Pierfederici, S.; Rael, S.; Davat, B. High Voltage Ratio DC–DC Converter for Fuel-Cell Applications. *IEEE Trans. Ind. Electron.* **2010**, *57*, 3944–3955. [[CrossRef](#)]
20. Vinnikov, D.; Roasto, I.; Strzelecki, R.; Adamowicz, M. Step-Up DC/DC Converters With Cascaded Quasi-Z-Source Network. *IEEE Trans. Ind. Electron.* **2012**, *59*, 3727–3736. [[CrossRef](#)]
21. Jiexun, L.; Dawei, G.; Yue, W. High Power High Voltage Gain Interleaved DC-DC Boost Converter Application. In Proceedings of the 2015 6th International Conference on Power Electronics Systems and Applications (PESA), Hong Kong, China, 15–17 December 2015.
22. Zhidong, Q.; Jin, P.; Di, H. Pre-stage power converter of proton exchange membrane fuel cell based on fractional order PID controller. *Trans. China Electrotech. Soc.* **2019**, *34*, 236–243.
23. Abdelmalek, S.; Dali, A.; Bettayeb, M.; Bakdi, A. A new effective robust nonlinear controller based on PSO for interleaved DC–DC boost converters for fuel cell voltage regulation. *Soft Comput.* **2020**. [[CrossRef](#)]
24. Aljohani, T.M.; Ebrahim, A.F.; Mohammed, O. Hybrid Microgrid Energy Management and Control Based on Metaheuristic-Driven Vector-Decoupled Algorithm Considering Intermittent Renewable Sources and Electric Vehicles Charging Lot. *Energies* **2020**, *13*, 3423. [[CrossRef](#)]
25. Szymanski, J.R.; Zurek-Mortka, M.; Wojciechowski, D.; Poliakov, N. Unidirectional DC/DC Converter with Voltage Inverter for Fast Charging of Electric Vehicle Batteries. *Energies* **2020**, *13*, 4791. [[CrossRef](#)]
26. Rodríguez Licea, M.A. Fault Tolerant Boost Converter with Multiple Serial Inputs and Output Voltage Regulation for Vehicle-to-Aid Services. *Energies* **2020**, *13*, 1694. [[CrossRef](#)]
27. Wang, P.; Zhou, L.; Zhang, Y.; Li, J.; Sumner, M. Input-Parallel Output-Series DC-DC Boost Converter with a Wide Input Voltage Range For Fuel Cell Vehicles. *IEEE Trans. Veh. Technol.* **2017**, *66*, 7771–7781. [[CrossRef](#)]
28. Axelrod, B.; Berkovich, Y.; Shenkman, A.; Golan, G. Diode-capacitor voltage multipliers combined with boost-converters: Topologies and characteristics. *IET Power Electron.* **2012**, *5*, 873–884. [[CrossRef](#)]

**Publisher’s Note:** MDPI stays neutral with regard to jurisdictional claims in published maps and institutional affiliations.



© 2020 by the authors. Licensee MDPI, Basel, Switzerland. This article is an open access article distributed under the terms and conditions of the Creative Commons Attribution (CC BY) license (<http://creativecommons.org/licenses/by/4.0/>).